Thin-Film Engineering of Solution-Processable n-Type Silicon Phthalocyanines for Organic Thin-Film Transistors

Thin-film engineering of solution processable n-type silicon phthalocyanines for organic thin-film transistors

*Rosemary Cranston[1], Mário C. Vebber[1], Jônatas Faleiro Berbigier[2], Nicole A. Rice[1], Claire Tonnelé[3], Zachary Comeau[1,4], Nicholas T. Boileau[1], Adam J. Shuhendler[4], Frédéric Castet[5], Luca Muccioli,[5,6] Timothy L. Kelly[2], and Benoît H. Lessard[1]**

1. University of Ottawa, Department of Chemical and Biological Engineering, 161 Louis Pasteur, Ottawa, ON, Canada, K1N 6N5
2. University of Saskatchewan, Department of Chemistry, 110 Science Place, Saskatoon, SK, Canada, S7N 5C9
3. Donostia International Physics Center, 4 Paseo Manuel de Lardizabal, 20018 Donostia, Euskadi, Spain
4. University of Ottawa, Department of Chemistry & Biomolecular Sciences, Ottawa ON, Canada, K1N 6N5
5. Université de Bordeaux, Institut des Sciences Moléculaires, 351 Cours de la Libération, 33405 Talence, France
6. University of Bologna, Department of Industrial Chemistry, 4 Viale Risorgimento, 40136 Bologna, Italy

*Corresponding Author. E-mail: benoit.lessard@uottawa.ca

Abstract

Metal and metalloid phthalocyanines are an abundant and established class of materials widely used in the dye and pigment industry as well as in commercial photoreceptors. Silicon phthalocyanines (SiPcs) are among the highest performing n-type semiconductor materials in this family when used in organic thin-film transistors (OTFTs) as their performance and solid-state arrangement is often increased through axial substitution. Herein, we study eight axially substituted SiPcs and their integration into solution processed n-type OTFTs. Electrical characterization of the OTFTs, combined with atomic force microscopy (AFM), determined that the length of the alkyl chain affects device performance and thin-film morphology. The effects of high temperature annealing and spin coating time on film formation, two key processing steps for fabrication of OTFTs, were investigated by grazing-incidence wide-angle x-ray scattering (GIWAXS) and x-ray diffraction (XRD) to elucidate the relationship between thin-film microstructure and device performance. Thermal annealing was shown to change both film crystallinity and SiPc molecular orientation relative to the substrate surface. Spin time affected film crystallinity, morphology, and interplanar *d*-spacing, and thus ultimately modifying device performance. Of the eight materials studied, bis(tri-*n*-butylsilyl oxide) SiPc exhibited the greatest electron field-effect mobility (0.028 cm^2/Vs, threshold voltage of 17.6 V) of all reported solution processed SiPc derivatives.

Introduction

Organic thin-film transistors (OTFTs) have been used in applications such as chemical and biological sensors,[1,2] wearable electronics,[3] and flexible displays.[4,5] A primary advantage of organic semiconductors is that inexpensive solution based processing techniques such as inkjet printing and spin coating can be used for low-cost, large area manufacturing.[6–9] High performing solution processable p-type polymeric and small molecule semiconductors have been studied in OTFTs, with reported hole mobilities (μ_h) in excess of 1 cm^2/Vs.[10–12] Conversely, n-type semiconductors are often air sensitive and insoluble, rendering them incompatible with high throughput and low-cost solution processing techniques.[13] To achieve high mobility solution processable transistors, non-conjugated side chains must be engineered to simultaneously increase solubility while providing close intermolecular packing, facilitating the formation of highly crystalline thin-films.[14–16] Substituted alkyl chains have previously been reported to increase the solution processability of both p-type conjugated polymer[14,17,18] and small molecule[6,19,20] semiconductors. Changes in thin-film morphology, which often result in related electrical performance changes in OTFTs, have been attributed to alkyl chain length, branching point, chain flexibility, and chain position.[16]

Metal and metalloid containing phthalocyanines (MPcs) are a versatile family of small molecule semiconductors with favourable chemical, thermal, and opto-electronic properties.[21] Silicon phthalocyanines (SiPcs) have recently attracted significant interest due to their ease of synthesis and chemical tunability, leading to their integration into optoelectronic devices,[22–24] but also in more exotic applications such as photodynamic therapy,[25,26] or near infrared photo polymerization.[27,28] By exploiting axial substituents which can change solid state organization, SiPcs have recently demonstrated μ_e of 0.54 cm^2/Vs in OTFTs, which is among the best reported performance for all MPc semiconductors.[29–31] Axial substituents can be used to change the solubility, crystal structure, and the energy of crystallization of a material, thus affecting thin-film formation and morphology. Recently, by taking advantage of these axial

substituents, we developed solution processable bis(tri-*n*-hexylsilyl oxide) SiPc and bis(tri-*n*-butylsilyl oxide) SiPc based n-type transistors.[32]

Among processing methods, spin coating is a widely used lab scale technique for the deposition of thin organic semiconductor films on flat substrates. Thin-film formation via spin coating occurs as the residual solvent evaporates, in the optimal case driving and leading to crystal nucleation and formation.[33] The effectiveness of spin coating is largely dependent on the crystallization kinetics of the semiconductor and the employed fabrication conditions.[33,34] Compared to lengthy evaporative methods, such as physical vapour deposition, this process occurs in seconds as the solvent is ejected from the film at high rotational speeds and can be applied to a wider range of materials, including polymers.[33] However, due to the rapid rate of film crystallization, consistent film morphology, uniform grain sizes, and edge-on molecular orientation can be difficult to achieve.[7] Fabrication parameters such as solvent viscosity, spin speed, and annealing time and temperature also affect the morphology, packing, and crystallinity of spin coated thin-films.[6,33] Chou et al., found that when processing 6,13-bis(triisopropylsilylethynyl)-pentacene semiconductor solutions, slower spin speeds increase solvent evaporation time, which led to increased film crystallinity and improved μ_h.[33] Additionally, Zhang et al., reported how thermal annealing can tune the grain size of branched alkyl chain naphthalene diimides fused with 2-(1,3-dithiol-2-ylidene)malononitrile groups to achieve a higher μ_h.[6] It is therefore critical to study the effect of processing on film formation and to be cognizant that even small changes in molecular structure can have significant effects on final device performance.

Herein, the characterization of six axially-substituted bis(tri-alkylsilyl oxide) SiPcs are reported in bottom-gate top-contact (BGTC) solution processed OTFTs; previously studied bis(tri-*n*-hexylsilyl oxide) SiPc and bis(tri-*n*-butylsilyl oxide) SiPc are also included for comparison (**Figure 1**). The semiconducting properties of each material were evaluated by the crystal structures through density functional theory (DFT) calculations and in thin films by experimental electrical characterization of transistors. The effects of processing and molecular structure were elucidated through post-deposition

characterization by atomic force microscopy (AFM), grazing-incidence wide-angle x-ray scattering (GIWAXS) and x-ray diffraction (XRD). The findings of this study will be critical in the development of MPc-based solution-processable OTFTs.

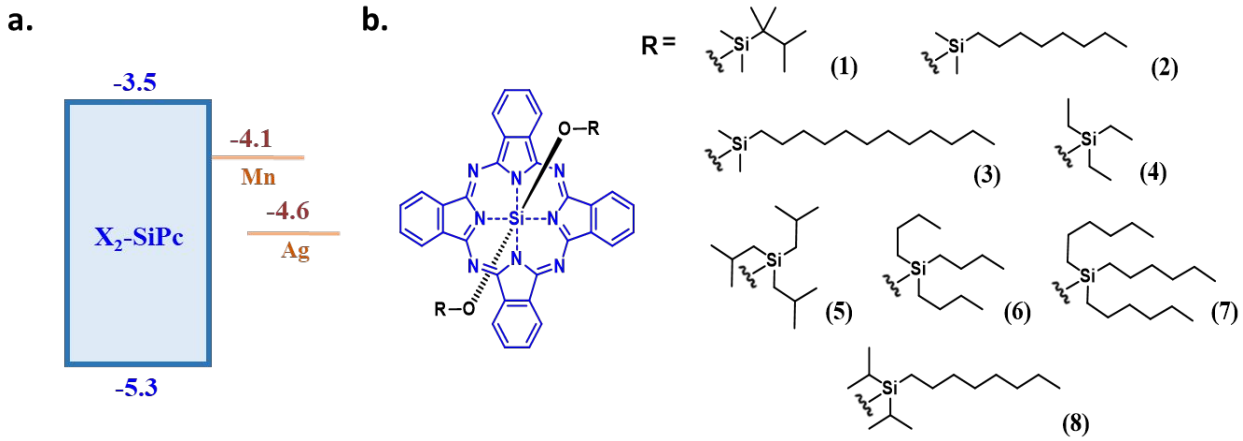

Figure 1. (a) Energy level diagram of X_2-SiPc, manganese (Mn),[35] and silver (Ag).[35] (b) Structure of X_2-SiPc with axial groups used in this study.

Results and Discussion

Quantum Chemical Calculations

DFT calculations were performed at the B3LYP/6-31G(d) level to determine energy levels and charge transport parameters of each material. **Table 1** collects the HOMO, LUMO, and LUMO+1 energies, along with the electron affinities (EAs), TD-DFT transition energies and oscillator strengths towards the two nearly-degenerate singlet excited states S_1 and S_2, and charge transfer internal reorganization energies (λ) calculated for the eight phthalocyanine molecules. The EAs calculated in the gas phase lie in the range of 1.93-2.07 eV, with a weak dependence on the chemical nature of the axial substituents. Note that theoretical values systematically underestimate compared to experimental ones obtained from measurements on thin films, in which local charges are stabilized by the polarizable environment.[36] LUMO and LUMO+1 energies, as well as the S_1 and S_2 excited states are expected to be degenerate for unsubstituted MPcs[37] or substituted X_2-MPcs with a centrosymmetric structure. In crystalline environments, geometrical distortions due to intermolecular interactions and positioning of

the axial substituents reduce the symmetry of the wave function and partially lift the degeneracy of the two LUMOs. However, the two levels remain very close and can both contribute to electron transport, in practice doubling the number of available pathways. Moreover, internal reorganization energy values for the bimolecular electron transfer process $MPc^- + MPc \rightarrow MPc + MPc^-$ are rather favorable (the lower the better, see rate **Equation 6**), with values particularly low for small-sized molecules, and only 50-100 meV higher than those of typical fullerene and non-fullerene acceptors with much larger aromatic cores.[38]

Table 1. DFT energy values of the HOMO, LUMO, LUMO+1, electron affinity (EA, obtained from differences in the total energies of the charged and neutral molecules in their optimized geometries), internal reorganization energies (λ) and TD-DFT vertical transition energies (ΔE_{01} and ΔE_{02}), and oscillator strengths (f_{01} and f_{02}) from the ground state S_0 towards the nearly-degenerate singlet states S_1 and S_2, calculated at the B3LYP/6-31G(d) level. All energy values are in eV.

Material	E_{HOMO}	E_{LUMO}	E_{LUMO+1}	EA	ΔE_{01} (f_{01})	ΔE_{02} (f_{02})	λ
1	-5.08	-2.88	-2.88	1.94	2.07 (0.35)	2.07 (0.35)	0.215
2	-5.06	-2.87	-2.86	1.94	2.07 (0.36)	2.07 (0.35)	0.251
3	-5.06	-2.87	-2.86	1.94	2.07 (0.36)	2.07 (0.35)	0.254
4	-5.07	-2.87	-2.87	1.93	2.06 (0.35)	2.07 (0.35)	0.213
5	-5.12	-2.94	-2.93	2.02	2.05 (0.33)	2.06 (0.32)	0.221
6	-5.12	-2.93	-2.92	2.03	2.05 (0.35)	2.06 (0.34)	0.241
7	-5.14	-2.95	-2.94	2.07	2.05 (0.36)	2.06 (0.34)	0.266
8	-5.09	-2.90	-2.90	1.98	2.06 (0.33)	2.06 (0.33)	0.213

Figure 2 depicts the top views of the molecular dimers giving rise to the largest electronic couplings (J_k), again calculated with DFT utilizing the experimental crystal structures. Numerical values of the main transfer integrals are collected in **Table S1** for all crystals. The electron mobilities, which depend on the square of the couplings (**Equation 6**), were estimated for each material in the hopping transport regime and the ideal case of zero energetic disorder along each crystallographic axis, and reported in **Table 2** together with the qualitative estimate of the dimensionality of transport. These values correspond to the maximum mobility achievable for a defect-free single crystal, and thus an upper limit to experimentally measured mobilities. All compounds show as expected[39] mainly 1D or partial 2D transport and in principle could exhibit decent mobilities in crystal phase, with **2**, **3**, and **6** showing the

most encouraging results, because of the larger electronic coupling (**Figure 2**). Conversely, **7**, **4**, and **8** show less promise than the others.

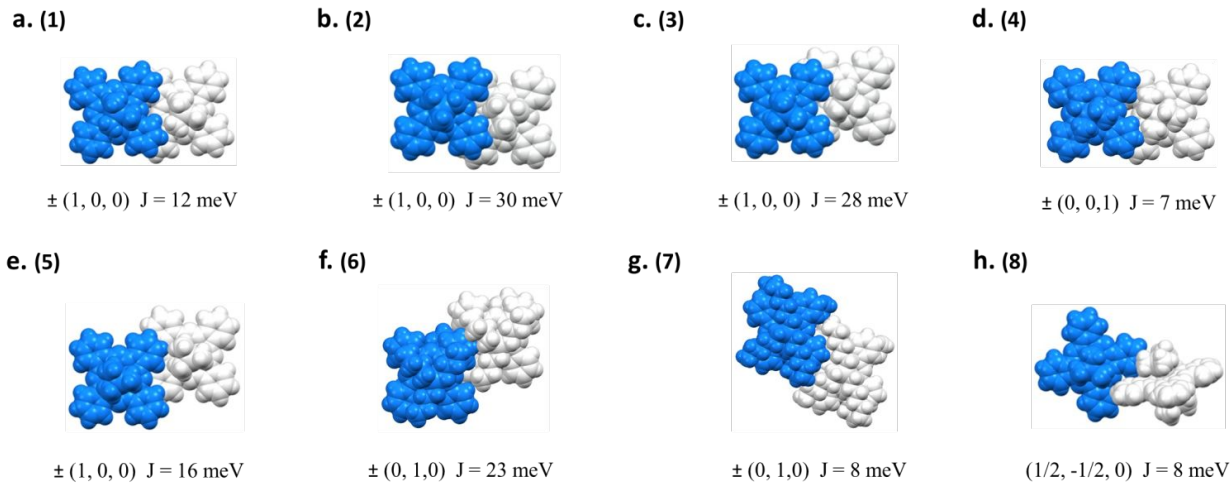

Figure 2. Top views of the molecular dimers giving rise to the largest electronic couplings, as extracted from periodic replicas of experimental crystal structures. In all structures, axial groups have been truncated to trimethyl silyl oxide for clarity.

Table 2. Computed electron mobilities along the crystal axes (μ_i with i = a, b, c; see **Equation 6**) in the eight phthalocyanine crystals, average mobility ($\mu_{e.avg} = (\mu_a + \mu_b + \mu_c) / 3$), and dimensionality (D) of the electron transport (ref 38).

Material	μ_a (cm^2/Vs)	μ_b (cm^2/Vs)	μ_c (cm^2/Vs)	$\mu_{e,\ avg}$ (cm^2/Vs)	D
1	0.300	0.112	0.034	0.149	2D
2	1.049	0.101	0.070	0.407	1D
3	0.914	0.115	0.009	0.346	1D
4	0.022	0.059	0.127	0.069	2D
5	0.532	0.030	0.029	0.197	1D
6	0.051	0.811	0.100	0.321	1D
7	0.012	0.092	0.054	0.053	2D
8	0.188	0.070	0.008	0.088	2D

Organic Thin-Film Transistor (OTFT) Performance

The eight axially substituted X_2-SiPcs described in **Figure 1** were used as the semiconductor in BGTC OTFTs. N-doped silicon wafers with a thermally grown silicon oxide dielectric layer were treated with trichloro(octyl)silane (OTS) to form an ordered monolayer surface to improve thin-film formation.[29]

The semiconducting layer was deposited by spin coating SiPc chloroform solutions on OTS treated wafers, followed by annealing at room temperature in air or at 100˚C under vacuum for 1 hour. Characterization was performed in nitrogen at atmospheric pressure, to determine the saturation regime electron field-effect mobility (μ_e) by **Equation 2**, threshold voltage (V_T), and on/off current ratio ($I_{on/off}$). **Figure 3** shows a characteristic transfer curve for each material that exhibits semiconducting characteristics in devices, alongside a diagram of the BGTC OTFT architecture used in this work.

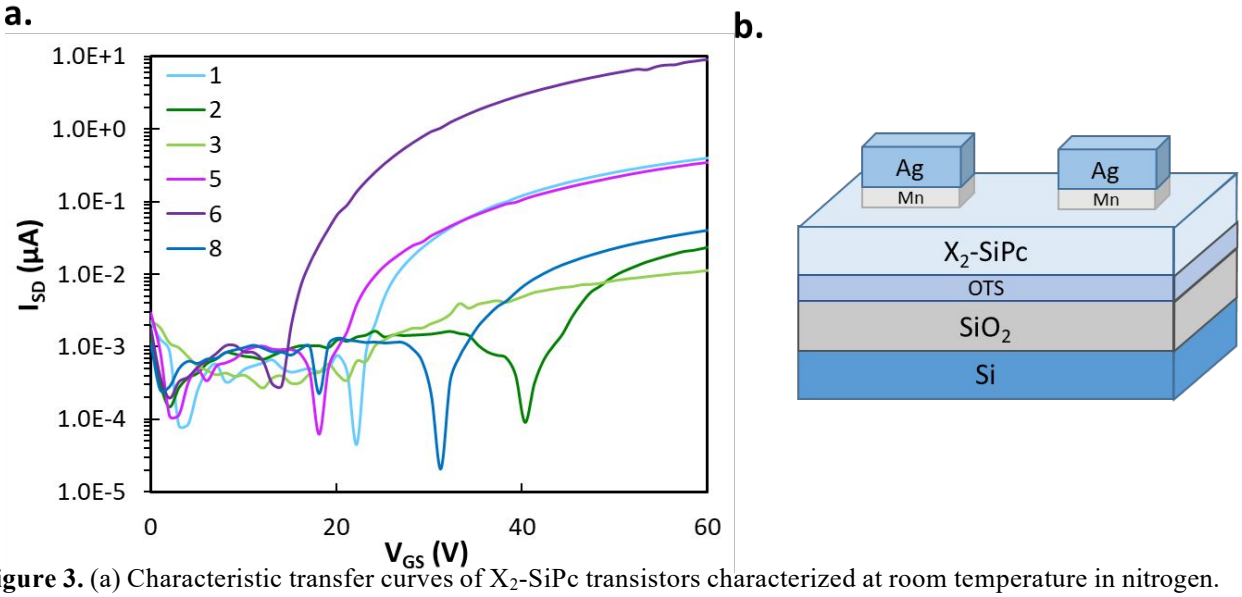

Figure 3. (a) Characteristic transfer curves of X_2-SiPc transistors characterized at room temperature in nitrogen. X_2-SiPc films were spun from chloroform at 1500 RPM for 90 s and annealed at 100˚C under vacuum for 1 hour. (b) Schematic diagram of bottom-gate top-contact OTFT architecture used in this study. **4** and **7** were found to be non-functional and are therefore excluded.

Electrical characteristics of each material for both annealing conditions are summarized in **Table 3**. **6** was found to have the highest $\mu_{e,\,avg}$ for both annealing at 25˚C and under vacuum at 100˚C of 7.3 x 10^{-3} cm^2/Vs and 2.8 x 10^{-2} cm^2/Vs, respectively. **6** also displayed the third lowest V_T of 32.6 V before annealing and the second lowest (17.6 V) after annealing at 100˚C. **4** and **7** were found to be non-functional as semiconductors in OTFTs with the fabrication conditions utilized in this study, as they did not exhibit semiconducting characteristics and therefore resulted in non-functional devices. This result is not completely unexpected given the low transfer integral values and correspondingly low calculated mobilities for these compounds (see **Table 2** and **Figure 2**). In literature, **7** was shown to be functional

in bottom-gate bottom-contact (BGBC) OTFTs fabricated by drop-casting and characterized using the same conditions, with an average μ_e of 7.3 x 10^{-6} cm^2/Vs.[32] In the same work, OTFTs made with **6** resulted in an average μ_e of 5.6 x 10^{-5} cm^2/Vs, three orders of magnitude lower than the value obtained in the present study (2.8 x 10^{-2} cm^2/Vs). These variations in electrical performance are unsurprising due to the differences in transistor architecture and semiconductor deposition, emphasizing the importance of optimization of fabrication conditions on the electrical performance of solution processable small molecule OTFTs.

Table 3. Summary of BGTC X_2-SiPc transistor characteristics, measured at room temperature in nitrogen atmosphere.

Material	Annealing Temp (°C)	$\mu_{e,\ max}$[a] (x 10^{-2} cm^2/Vs)	$\mu_{e,\ avg}$[b] (x 10^{-2} cm^2/Vs)	V_T[c] (V)	$I_{on/off}$[d]
2	25	0.208	0.137 ± 0.044	27.3 ± 1.6	10^4
	100	0.247	0.175 ± 0.025	24.9 ± 2.0	10^3
3	25	0.0322	0.0171 ± 0.0079	43.1 ± 1.2	10^2
	100	0.0321	0.0151 ± 0.014	42.4 ± 9.4	10^3
4	25	0.0300	0.0256 ± 0.0049	38.8 ± 0.3	10^2
	100	0.00320	0.00210 ± 0.00038	35.7 ± 10.4	10^2
6	25	-[e]	-[e]	-[e]	-[e]
	100	-[e]	-[e]	-[e]	-[e]
	25	0.141	0.0820 ± 0.021	22.8 ± 2.4	10^4
	100	0.202	0.163 ± 0.023	16.8 ± 2.4	10^4
7	25	0.888	0.734 ± 0.094	32.6 ± 3.5	10^5
	100	4.34	2.80 ± 0.53	17.6 ± 2.3	10^5
8	25	-[e]	-[e]	-[e]	-[e]
	100	-[e]	-[e]	-[e]	-[e]
	25	0.0405	0.0284 ± 0.0091	39.1 ± 0.8	10^3
	100	0.0356	0.0111 ± 0.0023	30.6 ± 8.2	10^3

a. maximum saturation regime electron field-effect mobility ($\mu_{e,\ max}$)
b. mean saturation regime electron field-effect mobility ($\mu_{e,\ avg}$)
c. mean threshold voltage (V_T)
d. on/off current ratio
e. non-functional device
Averages taken from 40 transistors excluding short circuits, with uncertainties calculated by the standard deviation.

As shown in

Table 3, annealing at 100˚C had little effect on the electrical characteristics of most of the SiPc transistors. For **1**, **2**, **5**, and **8**, the changes in μ_e and V_T are within the standard deviation and therefore no significant change in performance is correlated to annealing. However, for **6** the V_T decreased significantly by 15 V, with a μ_e increase of 2.1 x 10^{-2} cm^2/Vs after annealing. Interestingly, annealing at 100˚C resulted in an order of magnitude decrease (4.6 x 10^{-5} cm^2/Vs) in μ_e for **3**. AFM images of **3** and **6** before and after annealing are shown in **Figure S4**. Annealing **6** resulted in a more homogenous thin-film morphology compared to the non-annealed films, which could account for the observed increase in device performance. The effect of thermal annealing on **6** is further discussed in an upcoming section. After annealing, **3** exhibited a drastic morphology change with much larger plate-like features, potentially due to the exceptionally low crystallization temperature (89˚C reported in **Table S2**). These large features are typically ideal for charge transport;[6,7] however, the formation of large grain boundaries could in turn increase charge trapping, resulting in a lower μ_e.[40–42] Thermogravimetric analysis (TGA) and differential scanning calorimetry (DSC) was run on all X_2-SiPc derivatives. Melting and crystallization temperatures are reported in **Table S2**, and range from 61˚C 1 to 231˚C and 60˚C to 219˚C, respectively.

Thin-film Morphology

UV-Vis absorption spectroscopy of each compound in solution are identical (**Figure S5**) with no evidence of aggregation in solution.[43] When deposited as thin film on OTS functionalized glass a red-shift in absorption is observed with varying broadening and slight changes in peak maximum depending on choice of X_2-SiPc (**Figure S5**). The slight variation in absorption suggests different solid state arrangements. AFM was performed to correlate the effects of SiPc molecular structure, and corresponding thin-film morphology, to OTFT performance. Of the best performing semiconductors (**1**, **5**, and **6**), **1** and **6** show well-ordered homogenous film morphology with small cylindrical features (**Figure 4**). **5** exhibits larger interconnected features with more distinct grain boundaries compared to **6**. The elongated features and more densely packed films of these materials likely contribute to the high μ_e

exhibited in OTFTs. Of the worse performing materials (**2**, **3**, and **8**), **2** and **8** have a similar film morphology with small point-like features. Although these materials make homogenous films, they exhibit a much lower μ_e of 1.5 x 10^{-4} cm^2/Vs and 1.1 x 10^{-4} cm^2/Vs, and the two highest V_T of 42.4 V and 30.6 V, respectively. The spotted point-like features may represent more grain boundaries and increase charge trapping. As already mentioned, **3** has a unique morphology with very large plate-like features and large grain boundaries. These large grain boundaries have been shown to reduce charge carrier μ_e and result in worse electrical performance in OTFTs.[40–42,44] Accordingly, **3** shows the lowest μ_e of 2.1 x 10^{-5} cm^2/Vs and on/off current ratio of 10^2 as seen by the transfer curve in **Figure 3**. **4** and **7** resulted in films with the largest height differences (**Figure 4**) and poor grain interconnectivity, which corresponds to non-functional OTFTs.

As shown by **Figure 4**, the nature of the axial substituents greatly affects thin-film morphology, directly impacting transistor performance. The worst performing semiconductors (**2**, **3**, and **8)** have a longer alkyl chain, resulting in highly asymmetric axial substituents. These long chains may hinder molecular packing and subsequently charge transfer yielding poor semiconducting performance characteristics (**Table 3**). The importance of molecular packing and thin-film formation on device performance is highlighted through material **2**. From DFT calculations (**Table 2**), **2** exhibited the highest calculated $\mu_{e,\ avg}$, however displayed low μ_e and high threshold voltage in OTFTs, likely due to thin-film characteristics and morphology. Of the best performing semiconductors (**1**, **5**, and **6**), **1** and **5** have axial substituents with asymmetric short branched chains, whereas **6** has symmetric trialkyl linear chains six carbons in length. Since **6** exhibited the highest μ_e in OTFTs, this may suggest an optimum median chain length for linear trialkyl substituents which promotes molecular packing. The other symmetric trialkyl materials (**4** and **7**) were non-functional as semiconductors. Materials **4** and **7** may have been non-functional due to the length of their alkyl chains, resulting in poor crystal growth and non-uniform morphologies.

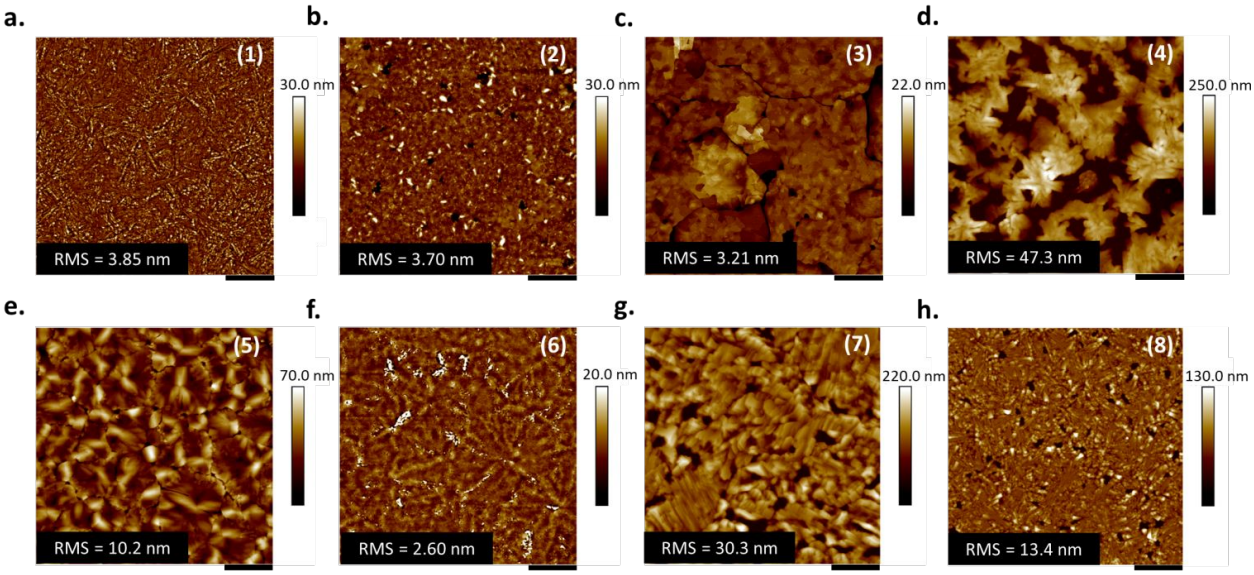

Figure 4. AFM images (10 µm x 10 µm) of materials 1 through 8 with a scale bar of 2.0 µm. All films were spun from chloroform at 1500 RPM for 90 s and annealed at 100˚C for 1 hour.

Effect of Annealing Temperature

Using **6** as the semiconductor, the effect of annealing on OTFT performance was further investigated by characterizing transistors annealed at different temperatures. The devices were annealed for 1 hour under vacuum at 100˚C or 185˚C, and compared to un-annealed devices which were left at room temperature in nitrogen. **Figure 5a** shows the change in μ_e and V_T with increasing annealing temperature. Annealing at 100˚C results in a μ_e increase of 2.1 x 10^{-2} cm^2/Vs from an initial value of 7.3 x 10^{-3} cm^2/Vs, with a V_T decrease of 15.0 V from an initial value of 32.6 V. However, upon annealing at 185˚C the μ_e decreases by 2.6 x 10^{-2} cm^2/Vs with a very large V_T increase of 39.8 V. As explained in the next section, the observed reduction in OTFT performance can be explained by changes in thin-film crystallinity and molecular orientation which do not favour charge transport.[33,40,44,45]

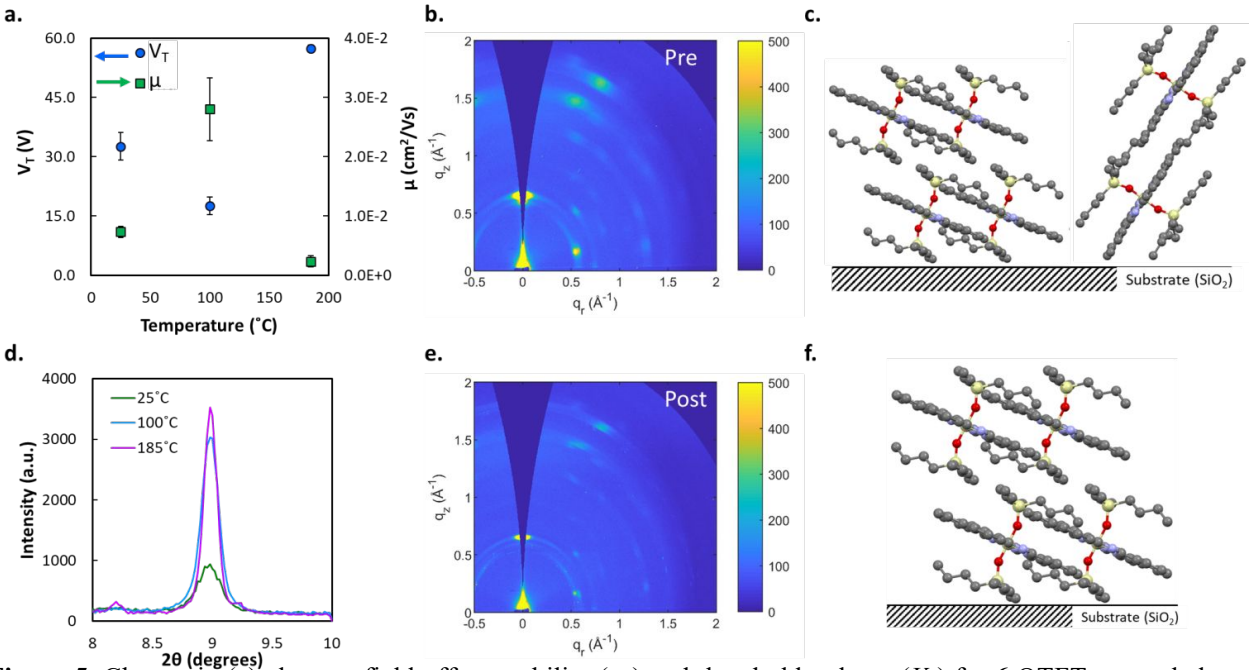

Figure 5. Change in (a) electron field-effect mobility (μ_e) and threshold voltage (V_T) for **6** OTFTs annealed at 25˚C, 100˚C, and 185˚C. (d) X-ray diffraction pattern of films. 2D scattering patterns for films annealed at (b) 25˚C α = 0.02° and (e) 185˚C α = 0.03° determined by GIWAXS. Diagram of (c) a combination of pseudo-face on and pseudo-edge on orientations, and (f) pseudo-face on orientation to the substrate determined by GIWAXS. All films were spun from chloroform at 1500 RPM for 90 s and annealed at the indicated temperature for 1 hour.

Through grazing-incidence wide-angle x-ray scattering (GIWAXS) the crystallinity and orientation of the molecules in relation to the substrate was analyzed before and after thermal annealing. **Figure 5b** shows the 2D scattering pattern of **6** when annealed at room temperature. The film is highly crystalline, with a structure strongly correlated to the single crystal as shown by the similarities in the diffraction patterns in **Figure S9**. The partial arcs observed throughout the pattern also indicate a high degree of preferential orientation with respect to the substrate.[44] The alignment of the (100) peak, q = 0.65 Å^{-1}, along the q_z axis indicates that one major molecular orientation is with the (100) plane preferentially aligned parallel to the substrate surface (pseudo-face on). The (010) peak at q = 0.60 Å^{-1} reveals additional information; there are two distinct partial arcs at χ = 0 and 74° (where χ is the angle between q and the q_z axis), indicating two distinct orientations relative to the substrate. In addition to the pseudo-face on orientation described previously, there is a secondary population in a pseudo-edge on orientation with the (010) plane oriented parallel to the substrate. The pseudo-face on and pseudo-edge

on orientations are depicted in **Figure 5c**, and all other features in the scattering pattern are consistent with these two orientations.

After annealing at 185˚C for 1 hour the scattering pattern shows a change in the degree of preferential orientation (**Figure 5e**), indicated by a narrowing of the partial arcs and a disappearance of the second (010) reflection along q_z. The narrower arcs show an overall stronger degree of preferential orientation, while the presence of only a single (010) reflection at $\chi = 74°$ shows that all crystallites are now in a pseudo-face on orientation (**Figure 5c**). **Figure 5d** shows the x-ray diffraction (XRD) pattern of **6** annealed at each temperature. As the annealing temperature increases the intensity of the peaks increase with a slight decrease in peak width. The sharper more intense peaks indicate a larger crystalline coherence length and a more crystalline film.[6,44,46] The increase in peak intensity from 25˚C to 100˚C indicates a more ordered crystalline film, which may correspond to the increase in μ_e and decrease in V_T observed in OTFT performance. In literature, annealing has been shown in the most favorable cases to improve film crystallinity, reduce intermolecular spacing, and decrease the number of film defects, thus increasing the μ.[6,47] For **6**, annealing had no effect on the intermolecular spacing between crystal planes as observed by the consistent peak location at $2\theta = 9°$. AFM images of the films show that the film morphology becomes more uniform with smaller vertical ridges after annealing at 100˚C (**Figure S4**), which supports the increase in device performance. However, after annealing at 185˚C OTFT performance decreases despite the further improvement in film crystallinity. Annealing at a high temperature may facilitate large crystallite formation that results in worse charge transfer, and therefore decreased electrical performance, due to grain-boundary effects.[47,48]

In addition to grain size dependency, the decrease in OTFT performance after annealing at 185˚C may be due to the molecular orientation relative to the substrate.[44] The disappearance of the (010) peak along the q_z axis at 185˚C indicates that, after annealing, there is a stronger preference for the SiPc molecules to align in the pseudo-face on orientation shown in **Figure 5f**. As indicated by the calculation results in **Table 1** and **Figure 2**, having all crystallites with the (100) planes parallel to the substrate is

undesirable for high μ_e OTFTs due to the lack of π-π stacking along this direction, resulting in ineffective charge transport from the source to the drain.[33,40,45] Therefore, the lower μ_e and higher V_T observed at a high annealing temperature is due to changes in film morphology and crystallite orientation. This result highlights a feature of materials with high mobility anisotropy (1D or 2D): since only specific crystal directions allow for efficient charge transport, increasing the crystallinity of the semiconducting film improves the transistor characteristics only if those directions lay parallel to the source-drain channel. Otherwise, more amorphous films can give rise to better performance.

Effect of Spin Time

In addition to annealing temperature, the effect of spin time on OTFT performance was investigated with OTFTs fabricated with deposition times of 30 s, 60 s, and 90 s, again using **6** as the semiconductor. **Figure 6a** demonstrates the change in μ_e and V_T with increasing deposition spin time. OTFTs fabricated at a longer spin time exhibited a small μ_e increase, of 2.9 x 10^{-3} cm^2/Vs from an initial μ_e of 4.4 x 10^{-3} cm^2/Vs, while experiencing a significant V_T reduction of 18.7 V from an initial value of 30.0 V, suggesting increased homogeneity of the semiconducting film and a decrease of surface traps at the interface with the dielectric.[49]

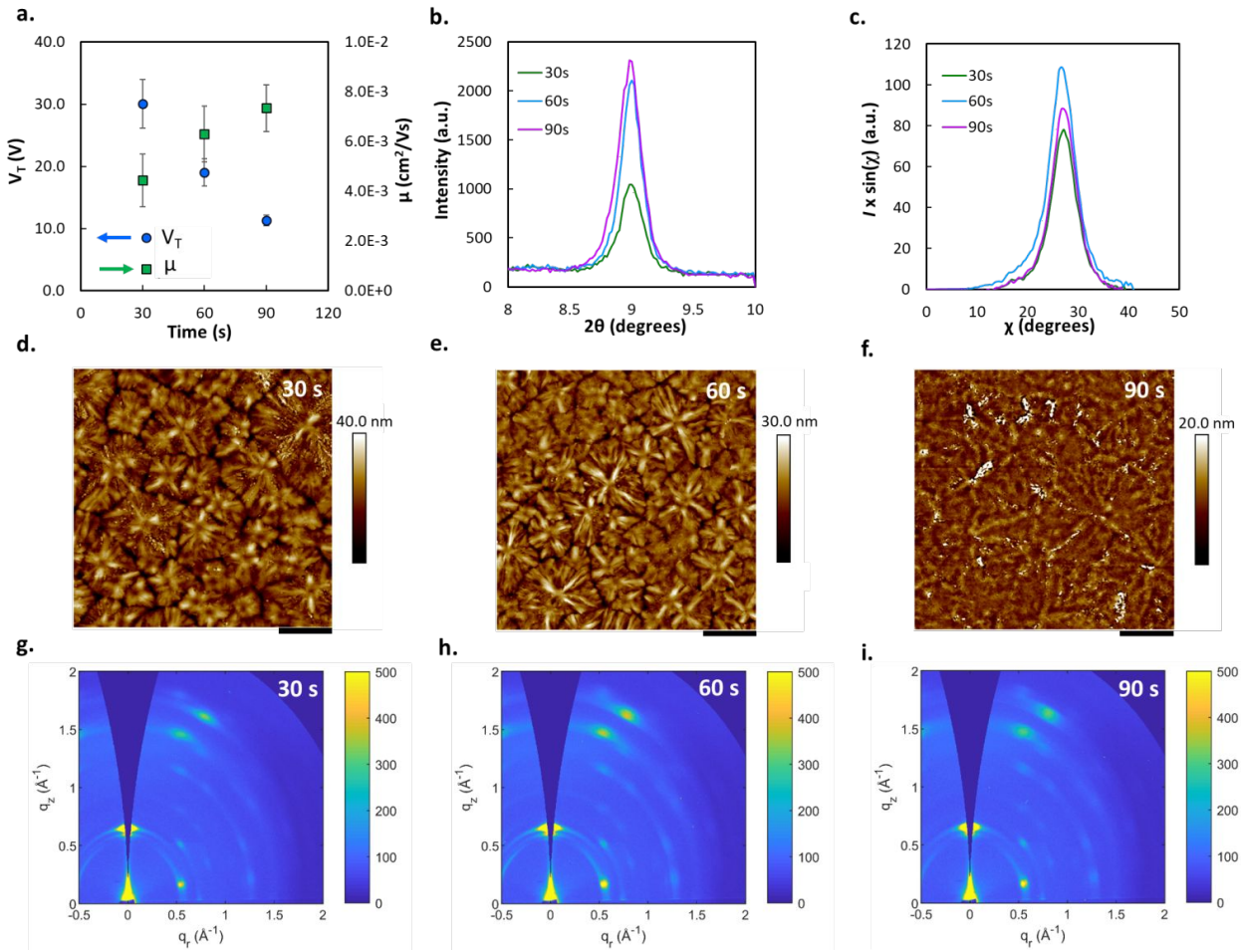

Figure 6. Change in (a) electron field-effect mobility (μ_e) and threshold voltage (V_T) for **6** OTFTs spun at 30 s, 60 s, and 90 s. (b) X-ray diffraction pattern of films. (c) Partial pole figures constructed from the (211) scattering feature, determined from GIWAXS data. AFM images (10 µm x 10 µm) of (d) 30 s, (e) 60 s, and (f) 90 s spin times with a scale bar of 2.0 µm. 2D scattering patterns for films spun at (g) 30 s α = 0.02°, (h) 60 s α = 0.03°, and (i) 90 s α = 0.03° determined by GIWAXS. All films were spun from chloroform at 1500 RPM for the indicated time and annealed at 25˚C.

AFM images (**Figure 6d-f)** show that as the spin time increases from 30 s to 90 s, the crystallites appear to reduce in size and become more homogenous, which corresponds to the observed improvement in OTFT performance. **Figures 6g-i** show the 2D scattering pattern of the films fabricated at each spin time determined by GIWAXS. Unlike annealing temperature, spin time has no effect on the preferred molecular orientation of the X_2-SiPc molecule relative to the substrate surface. The (100) and (010) peaks along the q_z axis are present at all spin times, indicating the presence of both pseudo-face on and pseudo-edge on orientations. Additionally, using the (211) peak as a reference (q = 1.8 Å^{-1}), there is little change in the distribution of crystallite orientations (**Figure 6c**).[44] The XRD patterns in **Figure 6b** show that a

longer spin time results in a greater (100) (2θ = 9°) peak intensity, therefore indicating a more crystalline thin film. However, the increase in peak intensity observed at a longer spin time may also be attributed to differences in film thickness. It can be concluded that increasing spin time up to 90 s results in a more homogenous film morphology while maintaining the same crystal orientation to the surface.

To further elucidate the effects of spin time on OTFT performance, additional characterization was performed with transistors fabricated using **3** as the semiconductor. **3** has very large axial substituents and a unique thin-film morphology, making it an interesting candidate for characterization. **Figure 7a** and **7b** show how μ_e and V_T change with increasing spin time. From 30 s to 60 s the μ_e trends upward with a small V_T increase of 3.2 V. However, in opposition to the trend observed for **6**, at 90 s μ_e decreases significantly by 5.3 x 10^{-4} cm^2/Vs from 7.8 x 10^{-4} cm^2/Vs with an increase in V_T of 8.7 V, from 24.5 V to 33.2 V.

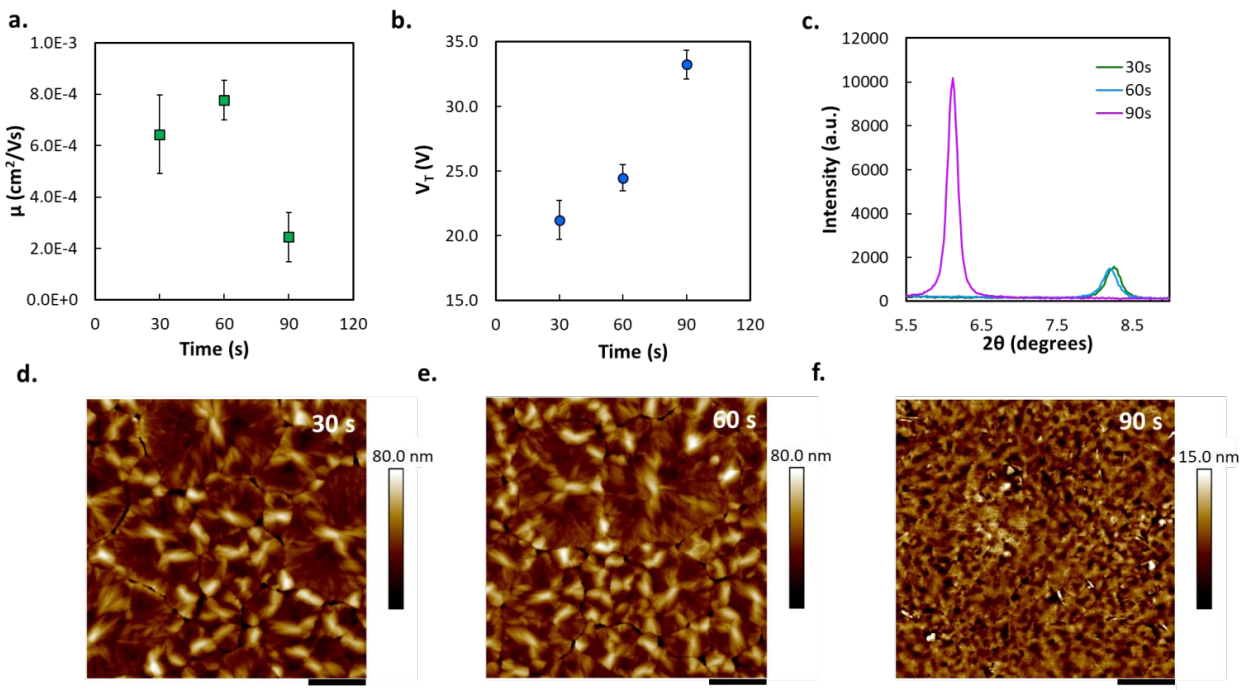

Figure 7. Change in (a) electron field-effect mobility (μ_e) and (b) threshold voltage (V_T) for **3** OTFTs spun at 30 s, 60 s, and 90 s. (c) X-ray diffraction pattern of films. AFM images (10 µm x 10 µm) of (d) 30 s, (e) 60 s, and (f) 90 s spin times with a scale bar of 2.0 µm. All films were spun from chloroform at 1500 RPM for the indicated time and annealed at 25˚C.

Figure 7c shows that the sudden variation in the device characteristics is associated with an abrupt change in the diffraction pattern of **3** spun at 30 s or 60 s to 90 s. The 30 s and 60 s trials exhibit peaks of similar intensity at $2\theta = 8.2°$, whereas for the 90 s trial this peak disappears and a new one with much higher intensity is present at $2\theta = 6.1°$. The distance between crystal planes was determined by **Equation 3** to be 10.8 Å for the 30 s and 60 s trials, and 14.4 Å for 90 s. The shift in peak location and interplanar spacing is likely a preference towards a different crystal polymorph, changing the molecular packing and the ability of the molecules to transfer charge, resulting in worse electrical performance in OTFTs spun for 90 s. This is further corroborated by the AFM images in **Figures 7d-f**, demonstrating that film morphology greatly changes at a spin time of 90 s. The 30 s and 60 s trials have similar sized and shaped features, which corroborates the similar electrical characteristics exhibited in OTFTs, while the 90 s trial has smaller features of a different shape compared to the 30 s and 60 s trials. Thus, it is likely that the larger grains and smaller interplanar spacing obtained at 30 s and 60 s improve charge transport through the film due to a decrease in charge trapping defects and enhanced π overlap between molecules.[6,7,50,51]

Furthermore, GIWAXS analysis of **3** spun at 90 s determined that the observed scattering pattern does not match the pattern predicted by the single crystal data (**Figure S7**), implying the formation of a different polymorph.[52] Consistent with the XRD data shown in **Figure 7c**, the 2D scattering pattern also shows a highly crystalline film; additionally, there is a high degree of preferential orientation, as exhibited by the strong speckle pattern in **Figure S7a**. The structural differences between single crystals and thin-films highlights once again the importance of fabrication methods and processing conditions on OTFT performance.

In the literature it has been demonstrated that crystal formation during spin coating occurs in two stages. First a short period of fast crystallization takes place, followed by a slower crystallization that depends on the spin speed.[33] Chou et al. demonstrated how spin speed influences the crystallization stages of BGTC 6,13-bis(triisopropylsilylethynyl) (TIPS)-pentacene OTFTs, and concluded that to achieve high

μ_h transistors a long period of slow crystallization is needed. It was hypothesized that longer spin time allows for an increased period of slow crystallization associated to residual solvent evaporation, which in turn promotes grain growth and defect healing, and increases device performance. For the X_2-SiPcs studied in this work, the length of the alkyl chain affects the crystallization kinetics due to differences in material properties (e.g. solubility, diffusivity and viscosity), and thus affects the duration of each crystallization stage. This is supported by the different results obtained for **3** and **6**. **6** exhibited reduced V_T and increased film crystallinity with increasing spin time, whereas **3** showed little change in OTFT performance and film morphology with the exception of the 90 s trial. At 90 s there is potentially more time to reach equilibrium and therefore a more stable polymorph can crystallize, which may result in the differences in device performance. Further investigation into the kinetics and stages of crystallization will help to understand how the processing conditions can be used to control thin-film formation of organic semiconductors for solution processable techniques.

Conclusions

In this work eight axially-substituted silicon phthalocyanines were compared as n-type semiconductors in bottom-gate top-contact OTFTs fabricated by spin coating. Six of these materials are reported in OTFTs for the first time. Bis(tri-*n*-ethyl oxide) and and bis(tri-*n*-hexylsilyl oxide) silicon phthalocyanines (**4** and **7**, respectively) were found to be non-functional as semiconductors in OTFTs, in line with DFT calculations on crystal structures indicating that the packing of these materials determines small electron transfer integrals. The transistors fabricated with all the other compounds showed promising performances, with electron mobilities in the 10^{-4}-10^{-2} cm^2/Vs range, and threshold voltages of a few tens of volts. After thermal annealing, bis(tri-*n*-butylsilyl oxide) SiPc (**6**) was found to have the highest μ_e of 0.028 cm^2/Vs, and the highest on/off current ratio of 10^5, making it the best performing semiconductor out of all reported solution processable SiPc materials.

For the best performing material (**6**), and for bis(*n*-dodecyldimethylsilyl oxide) SiPc (**3**) which showed a peculiar thin-film structure with large plate-like features, the correlation between morphology and transistor transfer properties was thoroughly investigated by means of AFM and x-ray scattering, as a function of two key preparation parameters, spin coating time and annealing temperature. It was demonstrated that for SiPcs thermal annealing can be used to control both film crystallinity and the orientation of the molecules relative to the substrate surface to possibly achieve higher μ_e OTFTs with reduced V_T. Additionally, spin time was shown to have the potential of being complimentary to annealing, since it can be used to tune thin-film crystallinity without affecting the orientation of the molecules. These encouraging results show the effectiveness of axial substitution as a strategy to control crystal packing and charge transport properties of SiPcs, and the potential of these materials as n-type semiconductors in OTFTs, whose performance can be optimized by exploiting the effects of fabrication conditions on thin-film structures.

Experimental

Materials

Bis(thexyldimethylsilyl oxide) silicon phthalocyanine (**1**), bis(*n*-octyldimethylsilyl oxide) silicon phthalocyanine (**2**), bis(*n*-dodecyldimethylsilyl oxide) silicon phthalocyanine (**3**), bis(tri-*n*-ethyl oxide) silicon phthalocyanine (**4**), bis(triisobutylsilyl oxide) silicon phthalocyanine (**5**), bis(tri-*n*-butylsilyl oxide) silicon phthalocyanine (**6**), bis(tri-*n*-hexylsilyl oxide) silicon phthalocyanine (**7**), and bis(diisopropyloctylsilyl oxide) silicon phthalocyanine (**8**) were synthesized as described in literature.[43]

OTFT Fabrication

OTFTs were fabricated on n-doped silicon substrates (15 mm x 20 mm) with a 300 nm thermally grown silicon oxide dielectric from Ossila. Substrates were first cleaned by sonication in sequential baths (5 min each) of soapy water, distilled water, acetone and methanol, then dried with nitrogen gas. Cleaned

substrates were treated with air plasma for 15 min. After which, substrates were rinsed with distilled water and isopropanol, then dried with nitrogen, before submersion in 1% v/v octyltrichlorosilane (OTS) in toluene for 1 hour at 70˚C. Upon removal from the silane surface treatment bath, substrates were rinsed with toluene and isopropanol and dried under vacuum at 70˚C for 1 hour. X_2-SiPc solutions were prepared in a nitrogen environment at a concentration of 10 mg/mL in chloroform. Solutions were heated at 50˚C for 1 hour, filtered through 0.2 μm pore size PTFE membranes, and deposited onto the substrates by spin coating 60 μL of solution at 1500 RPM for 90 s in nitrogen. The substrates were then annealed at room temperature in nitrogen or under vacuum at 100˚C for 1 hour. Top contact electrodes were formed using shadow masks with a channel width W = 30 μm and length L = 1000 μm, creating 20 individual transistors per substrate. 10 nm of manganese and 50 nm of silver were deposited through the masks by physical vapour deposition using an Angstrom EvoVac thermal evaporator with target rates of 0.5 Å/s and 1.0 Å/s respectively. Manganese was used as an electrode interlayer to reduce the contact barrier between the electrodes and semiconducting layer, resulting in lower threshold voltage and improved field-effect mobility.[53]

OTFT Characterization

OTFT electrical characterization was performed using a custom built automatic multi-tester. The tester is composed of 48 gold plated (20 nm) nickel probe tips which simultaneously make contact with the source-drain electrodes of the individual transistors, along with the gate electrode. Results were obtained from 40 individual transistors across two substrates fabricated by the method outlined above. The multi-tester introduces an approximate resistance of 750 mOhm to the testing apparatus. A Keithley 2614B and a MCC USB DAQ were used to control the source-drain voltage (V_{SD}) and gate voltage (V_{GS}) to obtain source-drain current (I_{SD}) measurements. The tester was kept in a controlled nitrogen environment at atmospheric pressure for the duration of characterization. By setting the V_{SD} constant at 50 V and varying the V_{GS}, I_{SD} measurements were obtained to determine the saturation regime field-effect

mobility, threshold voltage, and on/off current ratio. The following equation was used to relate the saturation regime field-effect mobility and threshold voltage to V_{GS} and I_{SD} measurements.

$$I_{SD} = \frac{\mu_e C_i W}{2L}(V_{GS} - V_T)^2 \quad (1)$$

Where μ_e is the field-effect mobility, V_T is the threshold voltage, W is the channel width, L is the channel length, and C_i is the capacitance density. The capacitance density was calculated by $C_i = (\varepsilon_0 \varepsilon_r)/t$, where t is the thickness of the dielectric (300 nm), and ε_r is the relative dielectric constant of SiO_2 equal to 3.9. The μ_e and V_T were determined by taking the square root of Equation 1 to obtain a linear relationship between $\sqrt{I_{SD}}$ and V_{GS} as shown by the following equation.

$$\sqrt{I_{SD}} = \sqrt{\frac{\mu_e C_i W}{2L}}(V_{GS} - V_T) \quad (2)$$

By plotting the square root of I_{SD} against V_{GS} the μ_e and V_T are determined by the slope and x-intercept, respectively. Lastly, the on/off current ratio is defined as the ratio of the highest and lowest currents measured in the characterized V_{GS} range.

Determination of Thermal Characteristics

TGA of X_2-SiPc samples were performed in nitrogen, at a 5˚C/min heating rate, with a Discovery 5500 equipment from TA instruments. DSC spectra were obtained with a Discovery 2500 equipment from TA instruments, where each sample was cycled between 0˚C to 250˚C three times with a heating/cooling rate of 5˚C min^{-1}.

Thin-Film UV-vis

Square glass microscope slides (25.4 mm, VWR) were cleaned in a sonication bath, following the same procedure described for silicon substrates. The clean slides were treated with air plasma (15 min) and then submerged in a 1% v/v OTS solution in toluene for 4 hours. After rinsing the substrates with isopropanol, the X_2-SiPc thin-films were deposited by spin coating 300 µL from

10 mg/mL chloroform solutions, at 500 RPM for 30s. Thin-film UV-vis spectra were then recorded in an Ocean Optics Flame spectrophotometer.

Interplanar Spacing

The interplanar spacing (*d*-spacing) between lattice plans was calculated using Bragg's Law shown by the following equation.

$$n\lambda = 2dsin\theta \quad (3)$$

Where λ is the wavelength of the incident wave equal to 1.54056 Å, d is the spacing between planes, θ is the angle of incidence in degrees, and n is a positive integer equal to 1 for this study.

Computational

All molecular geometries were optimized using density functional theory (DFT) with the B3LYP functional and the 6-31G(d) basis set. Each structure was verified to be a minimum of the potential energy surface on the basis of its all real harmonic vibrational frequencies. Internal reorganization energies (λ_i) were calculated at the same level, using the expression derived from the four-point adiabatic potential approach.

$$\lambda_i = E^{(-)}(M) - E^{(0)}(M) + E^{(0)}(M^-) - E^{(-)}(M^-) \quad (4)$$

Where $E^{(0)}(M)$ and $E^{(-)}(M^-)$ denote the ground-state energy of the neutral state and of the negatively charged state, respectively; $E^{(-)}(M)$ is the energy of the neutral molecule in the optimized geometry of the anion and $E^{(0)}(M^-)$, the energy of the anion in the optimized geometry of the neutral molecule. Transition energies towards the few first optically allowed excited states were also computed by means of time-dependent DFT at the B3LYP/6-31G(d) level.

Transfer integrals (J_k) characterizing the electron coupling between molecular pairs (k) were obtained by employing the projection method involving the LUMOs of monomers.[54] Since all molecules possess nearly degenerate LUMO (L) and LUMO+1 (L+1) levels which both contribute to the transport,

the effective transfer integrals for electron transport were computed as geometric averages in line with previous works.[39]

$$J_k = \frac{1}{\sqrt{2}}\{J^2_{L,L} + J^2_{L+1,L} + J^2_{L,L+1} + J^2_{L+1,L+1}\}^2 \quad (5)$$

The relative electron mobilities along the crystal axes i = *a, b, c* were evaluated at zero field neglecting energetic disorder in the transport level energies, using the expression:

$$\mu_i = \frac{q}{h}\left(\frac{\pi}{k_B T}\right)^{3/2} \frac{1}{\sqrt{\lambda}} \exp\left(-\frac{\lambda}{4k_B T}\right) \sum_k J^2_k (\vec{r}_k \cdot \vec{e}_i)^2 \quad (6)$$

where the sum runs over all pairs of molecular neighbours separated by the distance vector $\vec{r}_k$, $\vec{e}_i$ is a cell axis unit vector. Variables q, h and k_B are respectively the elementary charge, the Planck, and Boltzmann constants, and T = 300 K. Equation 6 combines Marcus formula for the hopping rate (ν_k) between two neighbouring sites with the equation for the diffusion coefficient in one dimension, $D = \frac{1}{2}\sum_k \nu_k (\vec{r}_k \cdot \vec{e}_i)^2$, and Einstein's equation relating mobility with diffusion, $\mu = \frac{qD}{k_B T}$.[55] Quantum chemical calculations were performed with the ORCA[56] and Gaussian[57] programs.

GIWAXS

GIWAXS experiments were performed at the Canadian Light Source (CLS) using the Hard X-ray MicroAnalysis (HXMA) beamline. A photon energy of 12.69 keV was selected using a Si(111) monochromator. The beam size was defined by slits having a 0.2 mm vertical gap and a 0.3 mm horizontal gap, and the angle of incidence was set in the range of 0.02 – 0.07°, as indicated. The sample was deposited on a ⟨100⟩ silicon wafer by spin coating from chloroform at 1500 RPM. GIWAXS patterns were collected with a Rayonix SX165 CCD detector (80 μm pixel size; 16.3 cm diameter), which was placed 214 mm from the sample center. The GIWAXS data were calibrated against a silver behenate standard and analyzed using the GIXSGUI software package.[58] Both polarization and solid-angle corrections were applied.

AFM

AFM images were taken using a Bruker Dimension Icon AFM with ScanAsyst-Air tips. Tapping mode was used to collect all images with a scan rate of 1 Hz. Image processing and editing was performed with NanoScope Analysis v.1.8 software.

Acknowledgments

The Natural Sciences and Engineering Research Council of Canada (NSERC, RGPIN-2017-03732 to T.L.K.; RGPIN/2015-509 03987 and STPGP 506661-17 to B.H.L) and the University of Ottawa and the University of Saskatchewan are acknowledged for financial support. T.L.K. and B.H.L. are Canada Research Chairs. The research was undertaken, in part, thanks to funding from the Canada Research Chair program. The Canadian Light Source (CLS) is supported by CFI, NSERC, the University of Saskatchewan, the Government of Saskatchewan, Western Economic Diversification Canada, the National Research Council Canada, and the Canadian Institutes of Health Research. Technical support from HXMA beamline scientist Dr. Chang-Yong Kim is gratefully acknowledged. N.B also thanks NSERC for the PGS-D. Computer time was provided by the Mésocentre de Calcul Intensif Aquitain (MCIA) of the University of Bordeaux and financed by the Conseil Régional d'Aquitaine and the French Ministry of Research and Technology. We also thank Centre for Research in Photonics at the University of Ottawa (CRPuO) for access to the AFM and Dr. Ovens for performing single crystal x-ray diffraction on the SiPc derivatives.

References

1. Comeau, Z. J. *et al.* On-the-Spot Detection and Speciation of Cannabinoids Using Organic Thin-Film Transistors. *ACS Sensors* **4**, 2706–2715 (2019).

2. Boileau, N. T., Melville, O. A., Mirka, B., Cranston, R. & Lessard, B. H. P and N type copper phthalocyanines as effective semiconductors in organic thin-film transistor based DNA biosensors at elevated temperatures. *RSC Adv.* **9**, 2133–2142 (2019).

3. Someya, T. *et al.* A large-area, flexible pressure sensor matrix with organic field-effect transistors for artificial skin applications. *Proc. Natl. Acad. Sci. U. S. A.* **101**, 9966–9970 (2004).

4. Zhou, L. *et al.* All-organic active matrix flexible display. *Appl. Phys. Lett.* **88**, 2004–2007 (2006).

5. Gelinck, G. H. *et al.* Flexible active-matrix displays and shift registers based on solution-processed organic transistors. *Nat. Mater.* **3**, 106–110 (2004).

6. Zhang, F. *et al.* Critical Role of Alkyl Chain Branching of Organic Semiconductors in Enabling Solution-Processed N-Channel Organic Thin-Film Transistors with Mobility of up to 3.50 cm2 V−1 s−1. *J. Am. Chem. Soc.* **135**, 2338–2349 (2013).

7. Lee, S. S. *et al.* Controlling nucleation and crystallization in solution-processed organic semiconductors for thin-film transistors. *Adv. Mater.* **21**, 3605–3609 (2009).

8. Minemawari, H. *et al.* Inkjet printing of single-crystal films. *Nature* **475**, 364–367 (2011).

9. Forrest, S. R. Electronic Appliances on Plastic. *Nature* **428**, 911–918 (2004).

10. Li, J. *et al.* A stable solution-processed polymer semiconductor with record high-mobility for printed transistors. *Sci. Rep.* **2**, 754 (2012).

11. Paterson, A. F. *et al.* Addition of the Lewis Acid Zn(C6F5)2 Enables Organic Transistors with a Maximum Hole Mobility in Excess of 20 cm2 V−1 s−1. *Adv. Mater.* **31**, 1–8 (2019).

12. Mitsui, C. *et al.* High-performance solution-processable N-shaped organic semiconducting materials with stabilized crystal phase. *Adv. Mater.* **26**, 4546–4551 (2014).

13. Quinn, J. T. E., Zhu, J., Li, X., Wang, J. & Li, Y. Recent progress in the development of n-type organic semiconductors for organic field effect transistors. *J. Mater. Chem. C* **5**, 8654–8681 (2017).

14. Mei, J., Kim, D. H., Ayzner, A. L., Toney, M. F. & Bao, Z. Siloxane-terminated solubilizing side chains: Bringing conjugated polymer backbones closer and boosting hole mobilities in thin-film transistors. *J. Am. Chem. Soc.* **133**, 20130–20133 (2011).

15. Tsao, H. N. *et al.* Ultrahigh mobility in polymer field-effect transistors by design. *J. Am. Chem. Soc.* **133**, 2605–2612 (2011).

16. Lei, T., Wang, J.-Y. & Pei, J. Roles of Flexible Chains in Organic Semiconducting Materials. *Chem. Mater.* **26**, 594–603 (2013).

17. Sung, A., Ling, M. M., Tang, M. L., Bao, Z. & Locklin, J. Correlating molecular structure to field-effect mobility: The investigation of side-chain functionality in phenylene-thiophene oligomers and their application in field effect transistors. *Chem. Mater.* **19**, 2342–2351 (2007).

18. Osaka, I., Zhang, R., Kowalewski, T. & Mccullough, R. D. High-Lamellar Ordering and Amorphous-Like π-Network in Short-Chain Thiazolothiazole−Thiophene Copolymers Lead to High Mobilities. *J. Am. Chem. Soc.* **131**, 2521–2529 (2009).

19. Zhang, C. *et al.* Pursuing High-Mobility n-Type Organic Semiconductors by Combination of "Molecule-Framework" and "Side-Chain" Engineering. *Adv. Mater.* **28**, 8456–8462 (2016).

20. Gao, X. *et al.* Core-Expanded Naphthalene Diimides Fused with 2-(1,3-Dithiol-2-Ylidene)Malonitrile Groups for High-Performance, Ambient-Stable, Solution-Processed n-Channel Organic Thin Film Transistors. *J. Am. Chem. Soc.* **132**, 3697–3699 (2010).

21. A. Melville, O., H. Lessard, B. & P. Bender, T. Phthalocyanine-Based Organic Thin-Film Transistors: A Review of Recent Advances. *ACS Appl. Mater. & Interfaces* **7**, 13105–13118 (2015).

22. Pearson, A. J. *et al.* Silicon phthalocyanines as dopant red emitters for efficient solution processed OLEDs. *J. Mater. Chem. C* **5**, 12688–12698 (2017).

23. Zysman-Colman, E. *et al.* Solution-Processable Silicon Phthalocyanines in Electroluminescent

and Photovoltaic Devices. *ACS Appl. Mater. Interfaces* **8**, 9247–9253 (2016).

24. Dang, M. T. *et al.* Bis(tri-n-alkylsilyl oxide) silicon phthalocyanines: A start to establishing a structure property relationship as both ternary additives and non-fullerene electron acceptors in bulk heterojunction organic photovoltaic devices. *J. Mater. Chem. A* **5**, 12168–12182 (2017).

25. Zhang, Y., Ng, D. K. P. & Fong, W. P. Antitumor immunity induced by the photodynamic action of BAM-SiPc, a silicon (IV) phthalocyanine photosensitizer. *Cell. Mol. Immunol.* **16**, 676–678 (2019).

26. Ma, D. *et al.* Benzyl ester dendrimer silicon phthalocyanine based polymeric nanoparticle for in vitro photodynamic therapy of glioma. *J. Lumin.* **207**, 597–601 (2019).

27. Bonardi, A.-H. *et al.* Photoinduced Thermal Polymerization Reactions. *Macromolecules* **51**, 8808–8820 (2018).

28. H. Bonardi, A. *et al.* High Performance Near-Infrared (NIR) Photoinitiating Systems Operating under Low Light Intensity and in the Presence of Oxygen. *Macromolecules* **51**, 1314–1324 (2018).

29. Melville, O. A., Grant, T. M. & Lessard, B. H. Silicon phthalocyanines as N-type semiconductors in organic thin film transistors. *J. Mater. Chem. C* **6**, 5482–5488 (2018).

30. Yutronkie, N. J., Grant, T. M., Melville, O. A., Lessard, B. H. & Brusso, J. L. Old molecule, new chemistry: Exploring silicon phthalocyanines as emerging N-type materials in organic electronics. *Materials (Basel).* **12**, 1334 (2019).

31. Melville, O. A. *et al.* Ambipolarity and Air Stability of Silicon Phthalocyanine Organic Thin-Film Transistors. *Adv. Electron. Mater.* **5**, 1–7 (2019).

32. Grant, T. M., A. Rice, N., Muccioli, L., Castet, F. & H. Lessard, B. Solution-Processable n-Type Tin Phthalocyanines in Organic Thin Film Transistors and as Ternary Additives in Organic Photovoltaics. *ACS Appl. Electron. Mater.* **1**, 494–504 (2019).

33. Wei Chou, K. *et al.* Late stage crystallization and healing during spin-coating enhance carrier transport in small-molecule organic semiconductors. *J. Mater. Chem. C* **2**, 5681–5689 (2014).

34. Li, R. *et al.* Heterogeneous nucleation promotes carrier transport in solution-processed organic field-effect transistors. *Adv. Funct. Mater.* **23**, 291–297 (2013).

35. Hölzl, J. & Schulte, F. K. Work function of metals. in *Solid Surface Physics* 12–124 (Springer, 1979). doi:10.1007/bfb0048919

36. D'Avino, G. *et al.* Electrostatic phenomena in organic semiconductors: Fundamentals and implications for photovoltaics. *J. Phys. Condens. Matter* **28**, (2016).

37. Marom, N., Hod, O., Scuseria, G. E. & Kronik, L. Electronic structure of copper phthalocyanine: A comparative density functional theory study. *J. Chem. Phys.* **128**, 164107 (2008).

38. Swick, S. M. *et al.* Closely packed, low reorganization energy π-extended postfullerene acceptors for efficient polymer solar cells. *Proc. Natl. Acad. Sci.* **115**, E8341–E8348 (2018).

39. Manoj Gali, S., Matta, M., H. Lessard, B., Castet, F. & Muccioli, L. Ambipolarity and Dimensionality of Charge Transport in Crystalline Group 14 Phthalocyanines: A Computational Study. *J. Phys. Chem. C* **122**, 2554–2563 (2018).

40. Shi, Y. & Li, X. Solution-processable ambipolar organic field-effect transistor based on Co-planar bisphthalocyaninato copper. *Org. Electron.* **15**, 286–293 (2014).

41. Chang, P. C. *et al.* Film morphology and thin film transistor performance of solution-processed oligothiophenes. *Chem. Mater.* **16**, 4783–4789 (2004).

42. Oh, J. H., Liu, S., Bao, Z., Schmidt, R. & Würthner, F. Air-stable n -channel organic thin-film transistors with high field-effect mobility based on N, N′ -bis(heptafluorobutyl)-3,4:9,10-perylene diimide. *Appl. Phys. Lett.* **91**, (2007).

43. C. Vebber, M., M. Grant, T., L. Brusso, J. & H. Lessard, B. Bis (tri-alkylsilyl oxide) silicon phthalocyanines: understanding the role of solubility on device performance as ternary additives in organic photovoltaics. *Langmuir* **36**, 2612–2621 (2020).

44. Rivnay, J., C. B. Mannsfeld, S., E. Miller, C., Salleo, A. & F. Toney, M. Quantitative Determination of Organic Semiconductor Microstructure from the Molecular to Device Scale. *Chem. Rev.* **112**, 5488–5519 (2012).

45. Li, L., Tang, Q., Li, H. & Hu, W. Molecular Orientation and Interface Compatibility for High Performance Organic Thin Film Transistor Based on Vanadyl Phthalocyanine. *J. Phys. Chem. B* **112**, 10405–10410 (2008).

46. Giri, G. *et al.* Tuning charge transport in solution-sheared organic semiconductors using lattice strain. *Nature* **480**, 504–508 (2011).

47. Tantiwiwat, M., Tamayo, A., Luu, N., Dang, X.-D. & Nguyen, T.-Q. Oligothiophene Derivatives Functionalized with a Diketopyrrolopyrrolo Core for Solution-Processed Field Effect Transistors: Effect of Alkyl Substituents and Thermal Annealing. *J. Phys. Chem. C* **112**, 17402–17407 (2008).

48. Sung, C. F. *et al.* Flexible fullerene field-Effect transistors fabricated through solution processing. *Adv. Mater.* **21**, 4845–4849 (2009).

49. Mityashin, A. *et al.* Multiscale modeling of the electrostatic impact of self-assembled monolayers used as gate dielectric treatment in organic thin-film transistors. *ACS Appl. Mater. Interfaces* **6**, 15372–15378 (2014).

50. Youn, J. *et al.* Fused thiophene semiconductors: Crystal structure-film microstructure transistor performance correlations. *Adv. Funct. Mater.* **23**, 3850–3865 (2013).

51. Hutchison, G. R., Ratner, M. A. & Marks, T. J. Intermolecular charge transfer between heterocyclic oligomers. Effects of heteroatom and molecular packing on hopping transport in organic semiconductors. *J. Am. Chem. Soc.* **127**, 16866–16881 (2005).

52. Liman, C. D. *et al.* Two-dimensional GIWAXS reveals a transient crystal phase in solution-processed thermally converted tetrabenzoporphyrin. *J. Phys. Chem. B* **117**, 14557–14567 (2013).

53. Alfred Melville, O. *et al.* Contact Engineering using Manganese, Chromium and Bathocuproine in Group 14 Phthalocyanine Organic Thin-Film Transistors. *ACS Appl. Electron. Mater.* **2**, 1313–1322 (2020).

54. F. Valeev, E., Coropceanu, V., A. da Silva Filho, D., Salman, S. & Brédas, J.-L. Effect of Electronic Polarization on Charge-Transport Parameters in Molecular Organic Semiconductors. *J. Am. Chem. Soc.* **128**, 9882–9886 (2006).

55. Stehr, V., Pfister, J., Fink, R. F., Engels, B. & Deibel, C. First-principles calculations of anisotropic charge-carrier mobilities in organic semiconductor crystals. *Phys. Rev. B* **83**, 155208 (2011).

56. Neese, F. The ORCA program system. *Wiley Interdiscip. Rev. Comput. Mol. Sci.* **2**, 73–78 (2012).

57. Frisch, M. J. *et al.* Gaussian 16. (2016).

58. Jiang, Z. GIXSGUI: A MATLAB toolbox for grazing-incidence X-ray scattering data visualization and reduction, and indexing of buried three-dimensional periodic nanostructured films. *J. Appl. Crystallogr.* **48**, 917–926 (2015).